TU Delft

Delft University of Technology

Energy storage ultra porous carbon blacks by high temperature oxidation

Kelesidis, Georgios A.; Rossi, Nicola; Gungor, Ayca Senol; Prehal, Christian; Pratsinis, Sotiris E.

DOI
10.1016/j.powtec.2025.121557

Publication date
2026

Document Version
Final published version

Published in
Powder Technology

Citation (APA)
Kelesidis, G. A., Rossi, N., Gungor, A. S., Prehal, C., & Pratsinis, S. E. (2026). Energy storage ultra porous carbon blacks by high temperature oxidation. *Powder Technology*, *467*, Article 121557. https://doi.org/10.1016/j.powtec.2025.121557

Important note
To cite this publication, please use the final published version (if applicable).
Please check the document version above.

Copyright
Other than for strictly personal use, it is not permitted to download, forward or distribute the text or part of it, without the consent of the author(s) and/or copyright holder(s), unless the work is under an open content license such as Creative Commons.

Takedown policy
Please contact us and provide details if you believe this document breaches copyrights.
We will remove access to the work immediately and investigate your claim.

This work is downloaded from Delft University of Technology.
For technical reasons the number of authors shown on this cover page is limited to a maximum of 10.

Powder Technology 467 (2026) 121557

Contents lists available at ScienceDirect

Powder Technology

journal homepage: www.journals.elsevier.com/powder-technology

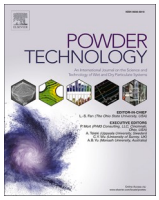

Energy storage ultra porous carbon blacks by high temperature oxidation

Georgios A. Kelesidis [a,b], Nicola Rossi [b], Ayca Senol Gungor [c], Christian Prehal [c,d], Sotiris E. Pratsinis [b,*]

[a] Faculty of Aerospace Engineering, Delft University of Technology, Kluyverweg 1, 2629 HS Delft, the Netherlands
[b] Particle Technology Laboratory, Institute of Energy & Process Engineering, Department of Mechanical and Process Engineering, ETH Zürich, Sonneggstrasse 3, 8092 Zürich, Switzerland
[c] Materials and Device Engineering Group, Department of Information Technology and Electrical Engineering, ETH Zürich, Gloriastrasse 35, 8092 Zürich, Switzerland
[d] Department of Chemistry and Physics of Materials, Paris-Lodron University Salzburg, Jakob-Haringer Strasse 2a, 5020 Salzburg, Austria

HIGHLIGHTS

- Ultra porous carbon blacks (CBs) are produced by high temperature oxidation.
- Oxygen diffuses & reacts with the bulk CB particle, disordering its nanostructure.
- The oxidized CB has high specific surface area, 2185 m^2/g, & pores of 2–8 nm radius.
- This porous CB enables superior supercapacitance than any commercial carbon.
- Judicious CB oxidation is essential to improve CB performance in energy storage.

GRAPHICAL ABSTRACT

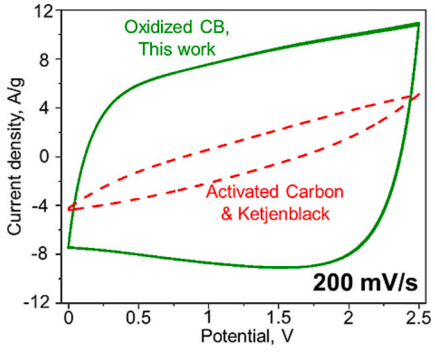

ARTICLE INFO

Keywords:
Carbon black
Oxidation
Porosity
Supercapacitors

ABSTRACT

Ultra porous carbonaceous nanoparticles were prepared by judicious oxidation of various commercial carbon blacks (CBs) at high temperatures (1200 °C). X-ray diffraction, N_2 adsorption and microscopy analyses revealed that during such oxidation, O_2 diffuses through and reacts with CB, disordering its crystalline structure. The concurrent external and internal oxidation of CB results in tiny pores that greatly increase the specific surface area, *SSA*, from 240 up to 2185 ± 199 m^2/g. This is about 150–200 % larger than the *SSA* of CB oxidized at low temperatures (450–550 °C), 50–100 % larger than the *SSA* of most porous CB commercially available and on par with that of commercial activated carbons (e.g. YP80). The potential of this ultra porous CB generated here for energy storage is showcased using electric double layer capacitors (EDLCs). The gravimetric capacitance of EDLCs using the above high *SSA* CB as active material is up to 60 % larger than those obtained from EDLCs based on YP80 or Ketjenblack at high scan rates (≥ 100 mV/s) and current densities of 0.02–5 A/g. The superior rate performance of these CBs is attributed to the high concentration of pores with a 2–8 nm radius formed largely by internal oxidation. Such pores cannot be produced at large concentrations by low temperature oxidation of CB that is used widely to enhance CB porosity. Hence, close control of the oxidation dynamics of CB can substantially increase supercapacitor performance.

* Corresponding author.
E-mail address: sotiris.pratsinis@ptl.mavt.ethz.ch (S.E. Pratsinis).

https://doi.org/10.1016/j.powtec.2025.121557
Received 12 November 2024; Received in revised form 6 August 2025; Accepted 13 August 2025
Available online 14 August 2025
0032-5910/© 2025 The Authors. Published by Elsevier B.V. This is an open access article under the CC BY license (http://creativecommons.org/licenses/by/4.0/).

1. Introduction

Porous carbonaceous materials are attractive for efficient energy storage using Li-ion batteries [1] and supercapacitors [2] due to their accessibility and relatively low cost. The potential of such materials is typically showcased for electric double layer capacitors (EDLCs) that are used for fast charging of Li-ion batteries and energy harvesting in hybrid/electric vehicles [3] and other transportation systems (e.g. trams, buses, aircrafts) [4]. The EDLC electrodes rely on porous carbonaceous materials to store charge electrostatically by electrosorption of electrolyte ions [5].

Currently activated carbon (AC) is mostly used in EDLCs due to its low cost and large porosity [4]. Porous ACs are commonly produced by gaseous [6] or wet [7] oxidation of coal [8], tar pitch [9] or biomass (e.g. coconut [10], walnut shells [11], lignin [12], carbon cloth [13]) particles. Oxidation of these particles results in a high fraction of small micropores (< 1 nm), decreasing the particle conductivity and area-normalized capacitance [14] but enhancing the particle specific surface area, *SSA* [8], as well as the gravimetric capacitance due to increased confinement [15]. So, EDLC electrodes are commonly produced using coconut shell ACs (e.g. YP80, Kuraray Co., Ltd) that have $SSA > 1800$ m^2/g and exhibit large specific capacitance, C_g, at current densities <1 A/g [16]. However, the C_g of such EDLCs generally decreases at higher current densities [16], which are most desirable for high power storage applications [17]. This can be attributed to the tortuosity of the micropores and particle size typically in the μm range of such ACs, limiting the access of electrolyte ions deep into the particle interior [18]. Carbonaceous particles with smaller primary particle sizes and with mesopores of 2–5 nm in size can improve the power density of EDLCs [18]. Scalable synthesis of such porous nanomaterials is essential to address the ever increasing energy storage demands [19].

In this regard, carbon black (CB) is the largest nanomaterial produced industrially today, having an annual worldwide production of 14.5 Mt. in 2022 [20]. It is manufactured by incomplete combustion of fossil fuels to form by surface reactions and coagulation ramified aggregates with high conductivity [21]. Such CB aggregates are often included as conductive additives (2–10 wt%) in EDLCs to reduce the equivalent series resistance as well as the electrolyte mass fraction [22]. The use of as-prepared (unoxidized) aggregated CB particles as an active material in supercapacitors is limited due to their small *SSA* and packing density [23] that result in thick electrodes with low C_g [14,24]. To this end, annealing [25] and oxidation [26] of CBs have been used even in large scale ovens [14] to enhance CB *SSA* and C_g. For example, CB oxidation at 10 vol% O_2 and 550 °C resulted in 2–8 nm in radius pores and increased the CB *SSA* [27] from 250 up to about 900 m^2/g. Ink-jet printing of such oxidized CB grades with large *SSA* enabled also the assembly of ultrathin EDLC electrodes [22]. So, oxidation at low temperatures can increase C_g of EDLC electrodes based on CB up to a factor of 36 [14]. The C_g of EDLC electrodes based on carbonaceous materials increases linearly with their *SSA* [24]. In this regard, the *SSA* of hollow CB particles produced by low temperature oxidation is, at least, 50 % smaller than that of commercial ACs (e.g. YP80). So, the performance of such hollow CB particles is not comparable to commercial ACs. Ketjenblack (ECP600JD, Nouryon) is currently one of the most porous CB grades available in the market, having $SSA = 1270–1445$ m^2/g [23,28]. So, Ketjenblack has been used as a conductive nanofiller in classic EDLCs [28] and as an active material in concrete-like supercapacitors [29]. However, the measured C_g from Ketjenblack EDLC electrodes [28] is still smaller than that obtained by coconut shell ACs with large *SSA* [16].

Recent advances in moving sectional [30] and lattice Monte Carlo [31] modelling have contributed to the design of CB with high *SSA* by internal and external oxidation. For instance, such oxidation [31] of CBs having a core-shell structure leads to hollow CB, explaining data from low temperature oxidation of Regal 600 [32] and Printex 95 [27] CB. In this regard, closely-controlled oxidation of CBs could further enhance their *SSA* [31] and thus their performance in EDLCs.

In this work, ultra porous CBs are generated thermogravimetrically by high temperature oxidation of commercial CBs capitalizing on the quantitative understanding of internal and external CB oxidation [31]. The porosity and crystallinity dynamics of the oxidized CB are monitored using X-Ray diffraction (XRD), N_2 adsorption and microscopy and compared to those of commercial ACs (Supelcarb, Sigma Aldrich & YP80) and Ketjenblack CB. The potential of the oxidized CB generated here for energy storage is showcased by assembling and characterizing EDLCs. The electrochemical performance of the oxidized CB is benchmarked against EDLCs made conventionally with Supelcarb, YP80 and Ketjenblack.

2. Methods

2.1. Oxidation of commercial CB grade

Commercial CB grades (Printex 95, Printex U, Printex G, Orion Engineered Carbons) with an average particle diameter of 15–50 nm were oxidized by thermogravimetric analysis (TGA) using a thermobalance (DSC 3+ STARe system, Mettler Toledo). About 40 mg of as-received CB were weighed in 600 μL alumina crucibles (Mettler Toledo). First, the samples were held at $T = 30$ °C for 30 mins in N_2. Then, the T was increased at 20 °C/min up to 1200 °C and held there for 10 min [27]. Afterwards, 10 vol% of O_2 in N_2 was flown through the TGA balance [27] and the CB mass decreased linearly with time (Supplementary Information: Fig. S1) consistent with TGA measurements of Printex 95 [27] and Regal 600 [32] oxidation. The CB mass conversion is obtained from the difference in CB mass before and after oxidation. Pure N_2 was introduced after 8, 16 and 24 mins to stop oxidation at 25, 50 and 75 % CB mass conversion, respectively. Then, T was decreased to 50 °C at 100 °C/min using the TGA thermobalance and kept there for 5 min to ensure the stability of the sample mass. The cooling rate used here is one order of magnitude smaller than those used during manufacture of furnace CB [33] and as such it should not affect the structural stability of CB. More than thirty samples were obtained by TGA using the procedure described above to collect enough sample mass for N_2 adsorption, XRD and microscopy as well as for preparation of the EDLC electrodes.

2.2. Characterization of CB and AC porosity and crystallinity

High-resolution transmission electron microscopy images were acquired from as-received and oxidized CBs, as well as commercial Ketjenblack (Nouryon), Supelcarb (Sigma Aldrich) and YP80 (Kuraray Co., Ltd) on a Tecnai F30 microscope (FEI) operated at 300 kV. All CBs and ACs were analyzed by N_2 adsorption on a Tristar II Plus surface area and porosity system (Micromeritics) at 77.3 K after degassing in vacuum (VacPrep 061, Micromeritics) at 200 °C overnight. In particular, the N_2 adsorption and desorption isotherms were obtained at relative pressure, $p/p_o = 0.05–0.99$, where p_o is the standard atmospheric pressure. The *SSA* was derived from the N_2 adsorbed at five p/p_o ranging from 0.05 to 0.25 using the Brunauer-Emmett-Teller (BET) method [34], while the area-based pore size distributions, micro-, meso- and macropore area and volume (Table S1) were obtained from the whole N_2 adsorption isotherm using the Barrett-Joyner-Halenda (BJH) method [35]. For completeness, the pore size distributions were also obtained using the density functional theory (DFT) method based on the manufacturer (Micrometrics) software (Fig. S2). So, the measured full isotherms were fitted to theoretical ones derived previously by DFT for N_2 adsorption in slit-shaped pores [36]. The pore size distributions measured for Supelcarb, Ketjenblack and oxidized CB using the BJH method are similar to those obtained using the DFT method. However, the smallest pores ($r_{pore} < 2$ nm) have been identified here using the BJH method.

The XRD patterns of CBs and ACs at diffraction angles, $2\theta = 10° - 70°$ were obtained using an AXS D8 diffractometer (Bruker) at a scan rate of 0.0197°/s. Here, the average interlayer distance, d, of CB was obtained by analysing the 002 XRD peak using Bragg's law [37]:

$$d = \frac{n \cdot \lambda}{2\sin\theta_{002}} \quad (1)$$

where $n = 1$ is the order of diffraction, $\lambda = 0.154$ nm is the wavelength of the diffractometer and θ_{002} is the angle of the 002 peak. Similarly, the average crystallite length, L_c, of CB was obtained by [37].

$$L_c = \frac{K \cdot \lambda}{\beta_{002}\cos\theta_{002}} \quad (2)$$

where $K = 0.89$ is the peak shape factor [37] and β_{002} is the full width of the half maximum of the 002 peak. The crystallite d and L_c were determined using Eqs. (1) and (2) with the θ_{002} and β_{002} derived from the measured XRD patterns. In specific, the CB θ_{002} and β_{002} were obtained by fitting a Gaussian distribution to the measured 002 peak [38].

Raman spectra of CB nanoparticles were obtained using a 515 nm laser having 50 mW power (Renshaw inVia). The laser was focused with a × 20 magnification optical microscope, which gives a 2 μm spot size, while a 10 % laser power was focused on the sample for 120 s and three acquisitions [39]. The intensities of the disorder (D ~ 1350 cm^{-1}) and graphitic (G ~ 1580 cm^{-1}) bands [39] were obtained after straight line subtraction of the baseline [40].

2.3. Preparation and characterization of EDLCs

Electrode pastes were prepared by mixing the active material, i.e. Supelcarb, YP80 or the oxidized CB produced here, with the conductive material (Ketjenblack) and polytetrafluoroethylene (PTFE, Sigma Aldrich) binder suspended in water (60 wt% concentration) at a mass ratio of 8:1:1 [16]. Electrode pastes containing only Ketjenblack and PTFE at a ratio of 9:1 were prepared to benchmark the EDLC performance of Ketjenblack as both active and conductive material. All pastes are rolled into a thin film and dried at ambient conditions overnight. The dried films are punched then into disc electrodes of 1.3 cm in diameter. The average electrode thickness, mass and density were measured and reported in Table S2. Prior to mass measurements and cell preparation, the electrodes are dried at 80 °C for 2 h under vacuum.

All custom-built coin-type EDLC cells were assembled in an argon filled glovebox (<1 ppm O_2, N_2 and H_2O) by placing two symmetric electrodes in a stainless steel case. The electrodes were placed on aluminum foils with 1.7 cm diameter, isolated by a 2 cm glass fiber separator (Whatman GF/A glass microfiber filters) and wetted using 120 μL of tetraethylammonium tetrafluoroborate dissolved in acetonitrile (1 M TEABF4 in AN). The latter is a standard organic electrolyte used to prepare supercapacitors based on carbonaceous materials [16]. Cyclic voltammetry (CV) and galvanostatic cycling with potential limitation (GCPL) measurements were conducted on the electrochemistry workstations (Biologic VMP3, EC-Lab). The CV curves were recorded with scan rates of 5–200 mV/s (4 cycles each rate). The equivalent GCPL measurements were done using $I = 0.02$ to 5 A/g at 0–2.5 V. The mass for the current normalization corresponds to the active material mass of a single electrode. The EDLC C_g was calculated based on the measured discharge time, Δt [41]:

$$C_g = 2\Delta t I / \Delta U \quad (3)$$

where ΔU is the operating voltage. A constant $\Delta U = 2.5$ V was used regardless of current density and without including the IR drop to avoid overestimating C_g.

3. Results and discussion

3.1. Porosity and crystallinity dynamics of CB during oxidation

Fig. 1 shows images (a-c), N_2 adsorbed per unit mass (d), measured (symbols) and predicted (lines & insets [31]) *SSA* (e), area-based pore size distribution (f) and XRD patterns along with the average d and L_c (g) of CB (Printex 95) oxidized at 10 vol% O_2 in N_2, 1200 °C and conversion, $\chi = 0$–75 %. In addition, lower magnification images that include more CB particles are given in Fig. S3.

As received (unoxidized) CB has a core-shell structure and contains only a few tiny pores that are not visible by microscopy (Fig. 1a) but can be quantified by N_2 adsorption (Fig. 1f: triangles). These CB particles contain a graphitic shell with lower reactivity than their amorphous core. This core-shell structure is not apparent in Fig. 1a but has been confirmed by high resolution microscopy [42], as well as by comparing *SSA* data to lattice Monte Carlo (LMC) simulations [31]. The porosity and crystallinity dynamics of this CB have been elucidated [27] during oxidation at 10 vol% O_2 in N_2 and low temperatures ($T < 1200$ °C). For example, at $T = 550$ °C, hollow CB particles are formed mostly by internal oxidation of the CB core [27]. At $T = 800$ °C, largely external oxidation decreases the particle diameter but does not affect its internal structure and porosity [27]. Most interestingly, oxidation at $T = 1200$ °C seems to disorder the CB internal structure and forms rather large pores (Fig. 1b, c).

The CB porosity dynamics during oxidation at these conditions were quantified using N_2 adsorption (Fig. 1d). The volume of the adsorbed N_2, v_N, increases with increasing χ, suggesting that CB becomes more porous by oxidation at 1200 °C. This is corroborated by the area-based pore size distributions obtained by the BJH [35] method (Fig. 1f). The area concentration of small pores with radius, $r_{pore} \leq 2$ nm increases up to $\chi = 50$ %. At $\chi = 75$ %, some of these small pores fuse to form larger ones ($r_{pore} \geq 3$ nm) while many more small ones are formed. The formation of such pores increases significantly the CB *SSA* from 240 m^2/g up to 2185 ± 199 m^2/g at $\chi = 75$ % (Fig. 1e: squares). The *SSA* evolution measured here is underestimated up to 65 % by lattice Monte Carlo simulations [31] for external and internal oxidation of core-shell CB (solid line). This underestimation indicates that as the graphitic shell of CB is oxidized at 1200 °C, its structure disintegrates and becomes more amorphous. In this regard, the measured *SSA* evolution is explained nicely by the oxidation dynamics derived for amorphous CB particles (broken line). This suggests that at 1200 °C oxidation takes place throughout the CB nanoparticle. This is partly explained by the XRD patterns of unoxidized and oxidized CB obtained here (Fig. 1g). As χ increases from 0 to 75 %, the d increases from 3.68 to 3.81 Å, while L_c hardly decreases from 1.4 to 1.3 nm. The latter is due to the increase of the mean crystallite size by the d enhancement. The increase of d and decrease of L_c nicely elucidate the defect formation in the CB crystal structure. The XRD patterns measured here are consistent with the d increase measured for coal-derived soot [43] oxidized at 1000–1200 °C. It indicates that oxidation at such high T disorders the graphitic shell structure of CB by enabling O_2 to diffuse and react with the bulk CB particle. This is further corroborated by the Raman spectra analysis (Fig. S4) showing that the disorder (D) over graphitic (G) band ratio, D/G, increases with χ increasing up to 50 %.

The oxidation of carbonaceous particles is sensitive to temperature and affects their internal nanostructure [27]. For example, oxidation at 550 °C makes CB more graphitic [27] by consuming the amorphous CB core leaving its graphitic shell intact. At 800 °C, oxidation takes place at the CB surface, reducing the particle size without affecting its internal nanostructure [27]. Here, microscopy, N_2 adsorption, XRD and Raman spectroscopy reveal that further increasing the oxidation temperature to 1200 °C results in amorphous CB. This enables O_2 to diffuse through the CB shell and react with the entire CB particle increasing significantly its porosity and *SSA*. This can be attributed to the large energy that is transferred to the CB particle by prolonged oxidation at high temperatures (i.e. large conversions) that causes substantial atomic displacements, as indicated by molecular dynamics simulations [44]. So, the oxidation mechanism of CB changes by increasing the temperature from 550 to 1200 °C altering its internal nanostructure.

It should be noted that oxidation increases the CB oxygen content introducing C-O and O-C=O functional groups on the particle surface [14]. In this regard, oxidation of CB for 5 h increased the oxygen content

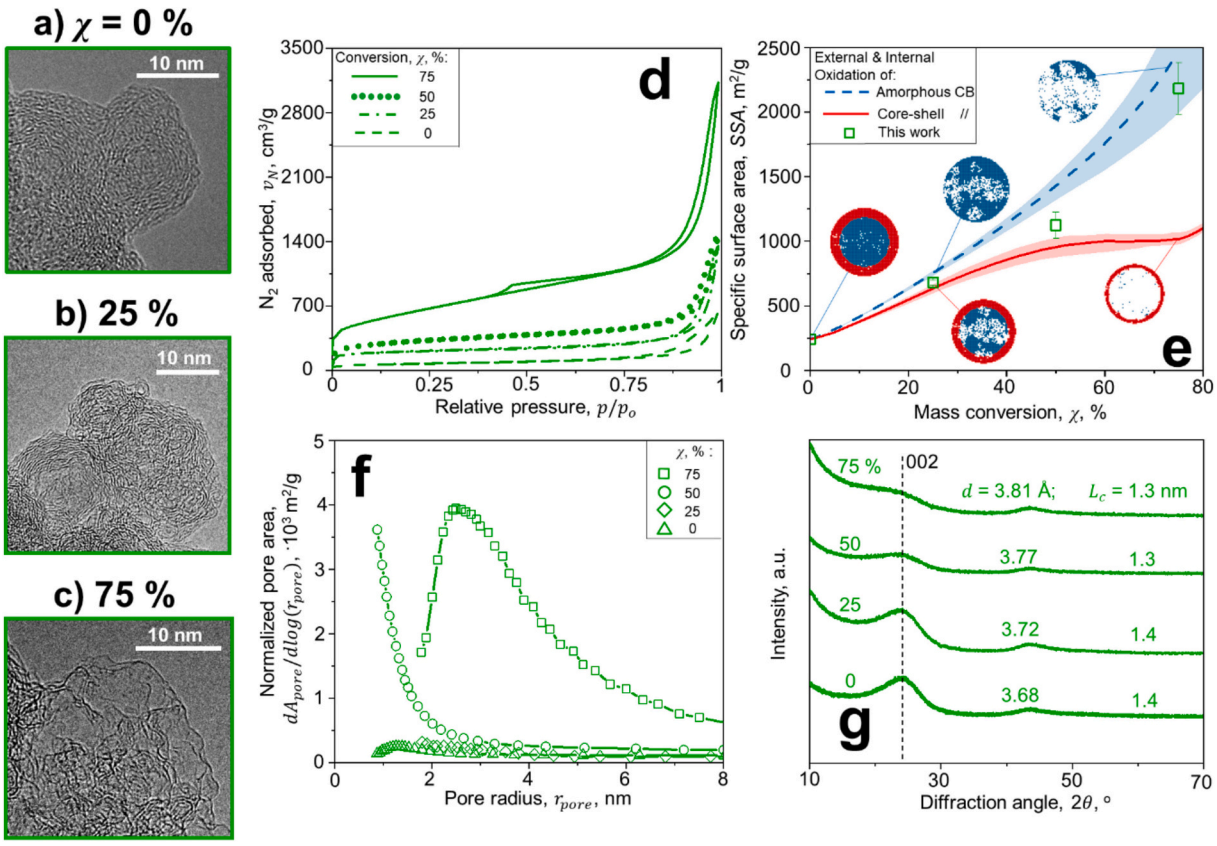

Fig. 1. Microscopy images (a-c), N_2 adsorbed per unit mass (d), measured (symbols) and predicted (lines & insets [31]) *SSA* (e), area-based pore size distribution (f) and XRD patterns along with the average d and L_c (g) of Printex 95 CB oxidized at 10 vol% O_2 in N_2, 1200 °C and conversion χ = 0–75 %. The measured *SSA* is also compared to that derived by lattice Monte Carlo [31] for amorphous (broken line) and core-shell CB (solid line).

by 10 % without deteriorating its cycle performance in supercapacitors [14]. Here, CB is oxidized for only up to 24 mins (Fig. S1). So the presence of any oxygenated functional groups should not affect its cycle performance.

The impact of high temperature oxidation was also quantified for other commercial CBs. Fig. 2 shows microscopy images of as-received (a-c) and oxidized (d-f) Printex 95 (a, d), Printex U (b, e) and Printex G (c, f) CBs along with their specific surface area, *SSA*. As-received Printex 95 is the finest CB among the grades investigated here having an average particle diameter, d_p = 15 nm and *SSA* = 240 m^2/g [45]. Printex G contains the largest CB particles with d_p = 51 nm and *SSA* = 44 m^2/g [45]. Oxidation at 1200 °C increases the *SSA* of all CB grades by a factor of 4–10. The oxidized CB *SSA* increases with decreasing d_p of the as-received CB. So, oxidized Printex 95 has the largest *SSA* (2185 ± 99 m^2/g) among all commercial CB grades and seems to be the optimal CB material. It should be noted that higher conversions might enhance *SSA* as has been shown theoretically [31] and experimentally [9]. However, these are accompanied typically by low yields that might be economically unattractive. For example, one of the highest *SSA* in the literature (2438 m^2/g) was attained at a yield of 6 % [9]. This *SSA* is marginally higher (~10 %) than that obtained here (2185 ± 199 m^2/g) at more than fourfold higher yield (25 %, Fig. 1e).

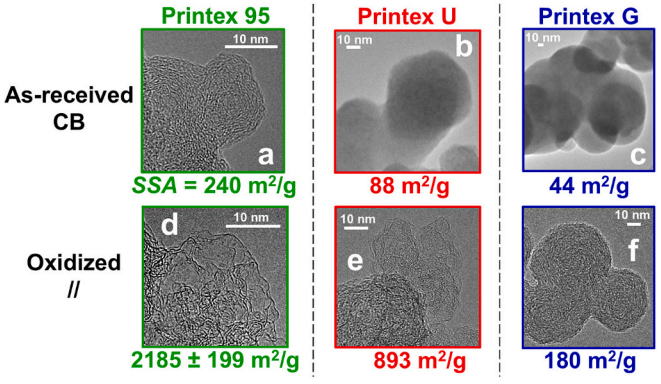

Fig. 2. Microscopy images of as-received (a-c) and oxidized (d-f) Printex 95 (a, d), Printex U (b, e) and Printex G (c, f) CBs along with their *SSA*.

3.2. Comparison of oxidized CB porosity to commercial CBs and ACs

Table 1 compares the *SSA* measured here for CB oxidized at T = 1200 °C and χ = 75 % to those obtained from the most porous CB grades commercially available. Printex XE2 (Orion Engineered Materials) and BP2000 (Cabot Corporation) are oxidized CB grades [23]. In specific, Printex XE2 contains hollow spheres generated by oxidation of CB grades at low T (500–600 °C) [27]. The SC3 grade produced by Cabot Corporation [22] has larger *SSA* than that of BP2000 but it is not currently available in the market. Ketjenblack is produced by shell gasification of coal tar [46]. These particles have *SSA* = 1270–1445 $m^2/$

Table 1
The *SSA* measured here for CB oxidized at T = 1200 °C and χ = 75 % is compared to those obtained from the most porous & commercially available CBs.

	Manufacturer	*SSA*, m^2/g
Printex XE2	Orion Engineered Materials [23]	1000
BP2000	Cabot Corporation [23]	1475
SC3	// // [22]	1880
Ketjenblack	Nouryon [23,28]	1270–1445
Oxidized CB	This work	2185 ± 199

g [23,28] and are widely used in supercapacitors as a conductive [28] or active [29] material. The *SSA* of 2185 ± 199 m^2/g measured here for CB oxidized at 1200 °C is the highest *SSA* among all porous CB grades commercially available. Furthermore, this *SSA* is 150–200 % larger than the *SSA* of CB oxidized at low temperatures (450 °C [14] - 550 °C [27]).

It should be noted that the porosity and *SSA* determined by N_2 or CO_2 adsorption vary with degassing time [47], temperature [48] and adsorption gas [49]. To this end, the porosity and *SSA* of the present oxidized CB are compared consistently to those measured by N_2 adsorption at identical conditions for commercial ACs (Supelcarb, YP80) and CB (Ketjenblack). Fig. 3 shows microscopy images (a-d), N_2 adsorption along with *SSA* (e) and area-based pore size distribution (f) measured here for two commercial ACs, Supelcarb and YP80, as well as for Ketjenblack in comparison to those of CB oxidized here at T = 1200 °C and χ = 75 %. The YP80 is produced by activation of coconut shells and used as an active material in supercapacitors [16]. Supelcarb is a carbonaceous molecular sieve used for filtration of hydrocarbons from the air [50]. Ketjenblack and the CB oxidized here contain disordered graphene layers that form rather large pores (> 2 nm). In contrast, Supelcarb and YP80 contain rather small micropores (< 2 nm) that are not visible by microscopy.

The porosity of ACs and CBs was quantified by N_2 adsorption (Fig. 3e). The obtained *SSA* of 2352.1 and 1356 m^2/g for YP80 and Ketjenblack, respectively, are in excellent agreement with those measured in literature for these materials [16,23,28] validating the present N_2 adsorption measurements. The adsorbed N_2 volume, $v_{N,}$ of ACs increases as the relative pressure, p/p_o, increases from 0 to 0.05. This confirms that the ACs are mostly microporous (r_{pore} < 2 nm) [51]. As p/p_o further increases to 1, the v_N remains constant at 100 and 700 cm^3/g for Supelcarb and YP80, respectively, in excellent agreement with the literature for N_2 adsorption of YP80 [16]. The lack of a hysteresis ring indicates that the present ACs do not contain any mesopores [51]. This is confirmed by the measured area-based pore size distribution (Fig. 3f). The YP80 and Supelcarb contain only a few pores with r_{pore} of about 2 nm. In contrast, the v_N measured for Ketjenblack and the oxidized CB generated here exhibit a hysteresis ring (starting around p/p_o = 0.4, Fig. 3e) proving that these CBs contain mesopores with r_{pore} = 2–8 nm, the optimal pore size range for supercapacitors [5]. In this regard, the oxidized CB produced here has the highest area concentration of such pores.

The micropore volume and area of Supelcarb, YP80, Ketjenblack and the oxidized CB are presented in Table S1. Supelcarb contains mostly micropores that result in a micropore volume of 0.358 cm^3/g. In contrast, Ketjenblack contains mostly meso- and macropores, having a negligible micropore volume of 0.001 cm^3/g. YP80 has a micropore volume of 0.17 cm^3/g, while its micropore area makes up 15 % of its total *SSA*. The oxidized CB has a similar micropore content with YP80 having a micropore volume of 0.066 ± 0.018 cm^3/g. The micropore area of the oxidized CB accounts for just 7 % of its total *SSA*.

3.3. Performance of EDLCs based on oxidized CB

The electrochemical energy storage performance of the present oxidized CB was quantified by preparing EDLCs benchmarked with commercial ACs and CB, a common practice for novel carbonaceous materials in supercapacitors [16]. All electrodes were compressed to attain the minimum thickness and maximum density with the present set up. The electrode thickness and density depend on the particle structure, as the film porosity increases with increasing particle sizes [52]. Ketjenblack primary particles have an average diameter of 37 nm and bond chemically with each other to form hard aggregates [53]. So, electrodes made here with Ketjenblack are 146.1 ± 6 μm thick resulting in a density of 0.25 g/cm^3 (Table S2). In this regard, oxidation of Printex 95 nanoparticles with a mean diameter of 15 nm at 1200 °C seems to disintegrate their aggregates and result in almost single graphene layers (Fig. 1c). This enables synthesis of thin electrodes, 97.5 ± 10.2 μm thick and 0.44 g/cm^3 density, on par with those made of YP80.

Fig. 4 shows the cyclic voltammograms obtained with scan rates of 5 (a) and 200 mV/s (b) for CB (solid lines & squares, this work) oxidized at the conditions of Fig. 3 to those of Supelcarb (dot-broken lines & triangles), YP80 (dotted lines, diamonds) and Ketjenblack (broken lines & circles). At 5 mV/s (Fig. 4a), all ACs and CBs exhibit a rather rectangular voltammogram, confirming the pure double layer capacitance mechanism for charge storage [5]. The discharge *I* exhibited by the oxidized CB

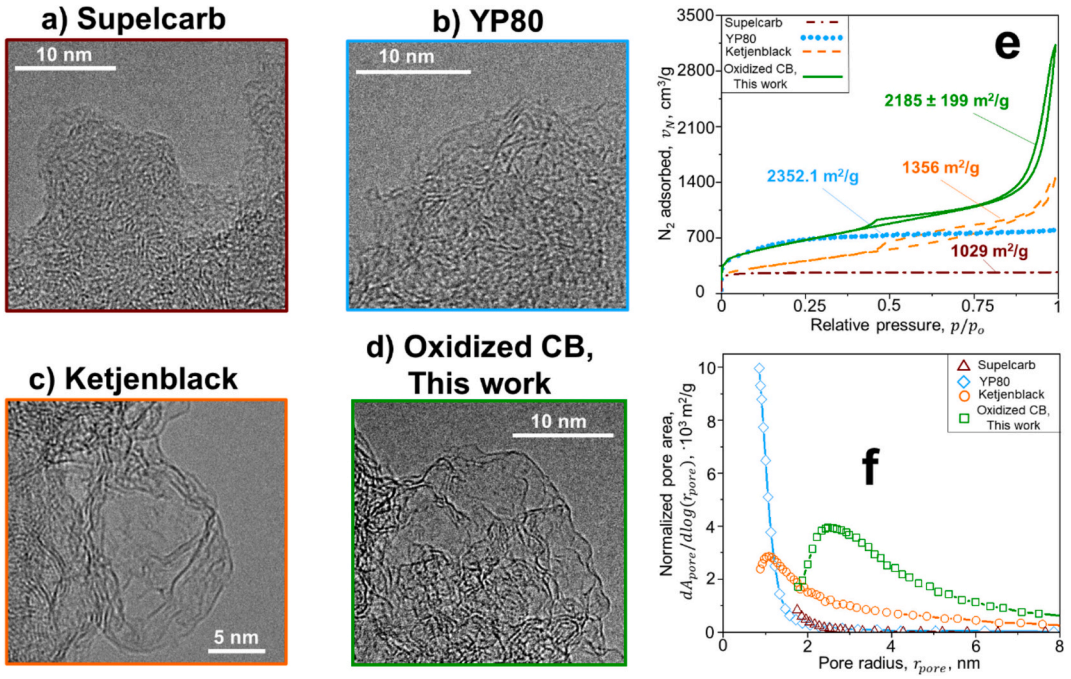

Fig. 3. Images (a-d), N_2 adsorbed per unit CB mass along with *SSA* (e) and area-based pore size distribution (f) measured for two commercial ACs, Supelcarb and YP80 as well as for Ketjenblack in comparison to those of Printex 95 CB oxidized at T = 1200 °C and χ = 75 %.

produced here is about twice larger than that of Supelcarb and on par (within 15 %) with those of YP80 and Ketjenblack. At scan rates of 50, 100 (Fig. S5) and 200 mV/s (Fig. 4b), however, the voltammograms obtained for the oxidized CB and Supelcarb retain their rectangular shapes, while those of YP80 and Ketjenblack are significantly distorted. This can be attributed to larger electronic and ionic resistance with the YP80 and Ketjenblack electrodes [54]. Furthermore, the maximum I exhibited by the oxidized CB at 200 mV/s is about 60 % higher than those of YP80 and twice larger than that of Ketjenblack and Supelcarb (Fig. S6). The cyclic voltammogram of oxidized CB obtained at 200 mV/s is stable over the four cycles tested here (Fig. S7).

Galvanostatic charge-discharge curves were obtained for EDLC electrodes at current densities, $I = 0.2$–5 A/g. As expected, the charge-discharge profiles obtained at $I = 0.2$ A/g are triangular for all ACs and CBs used here (Fig. 4c). Unlike the oxidized CB and Supelcarb, the YP80 and Ketjenblack exhibit small voltage drops (Fig. 4c). This indicates that the internal resistance of the oxidized CB produced here is smaller than those of YP80 and Ketjenblack [55]. The charge-discharge time obtained for the oxidized CB is more than twice larger than that of Supelcarb, about 25 % larger than that of Ketjenblack and 15 % smaller than that of YP80. Based on the measured charge-discharge times, the C_g is derived for $I = 0.2$–5 A/g (Fig. 4d).

Carbonaceous materials store electrical energy mainly through an electrochemical double-layer formed at the interface between electrode and electrolyte [2]. So, the C_g is determined by the pore surface area accessible to the electrolyte [56]. Organic electrolyte ions are larger than 1 nm [5] and cannot access the sub-nanometer micropores that are present in Supelcarb (Fig. 3f: triangles) resulting in low C_g (Fig. 4d: triangles). YP80 contains mostly 1 nm pores (Fig. 3f: circles & diamonds). There, an electrochemical double-layer can be formed only at small $I < 1$ A/g. So, the C_g of YP80 decrease at increasing I due to the limited electrochemical double-layer formation [18]. In contrast, Ketjenblack and the oxidized CB produced here contain 2–8 nm pores that ensure high effective diffusion coefficients for the electrolyte ions and facilitate the electrochemical double layer formation at the entire I range used here. However, the *SSA* of Ketjenblack is 42 % smaller than that of YP80 (Fig. 3e). This results in low I and C_g for supercapacitors based on Ketjenblack despite the presence of 2–8 nm pores. The oxidized CB has large *SSA* and retains its C_g at $I > 1$ A/g that is about thrice larger than that of Supelcarb and about 40 % larger than those of YP80 and Ketjenblack (Fig. 4d).

Commercial CB grades contain aggregated nanoparticles [21]. So, EDLC electrodes based on such commercial CBs have typically low density and exhibit low volumetric capacitance, C_v [23]. For example, the C_v measured here for electrodes based on Ketjenblack is 50–60 % lower than that with YP80 (Fig. S8). The present ultra porous oxidized CB contains nearly single graphene layers (Fig. 1c) that can be compacted to thinner films than those made with aggregated particles. As such they can be used for compact electrodes of high density (Table S2). As a result, the C_v of oxidized CB is twice as large as that of commercial Supelcarb and Ketjenblack at all I and practically on par with that of YP80.

So, the large *SSA* of the oxidized CB presented here enhances C_g and C_v at large current densities and scan rates. To the best of our knowledge, this is the first time shown that oxidized CBs can exhibit superior EDLC performance than commercial ACs. The robust EDLC performance of the oxidized CB produced here is similar to that obtained for activated graphite oxide with similar *SSA* and pore size distribution [57]. Instead

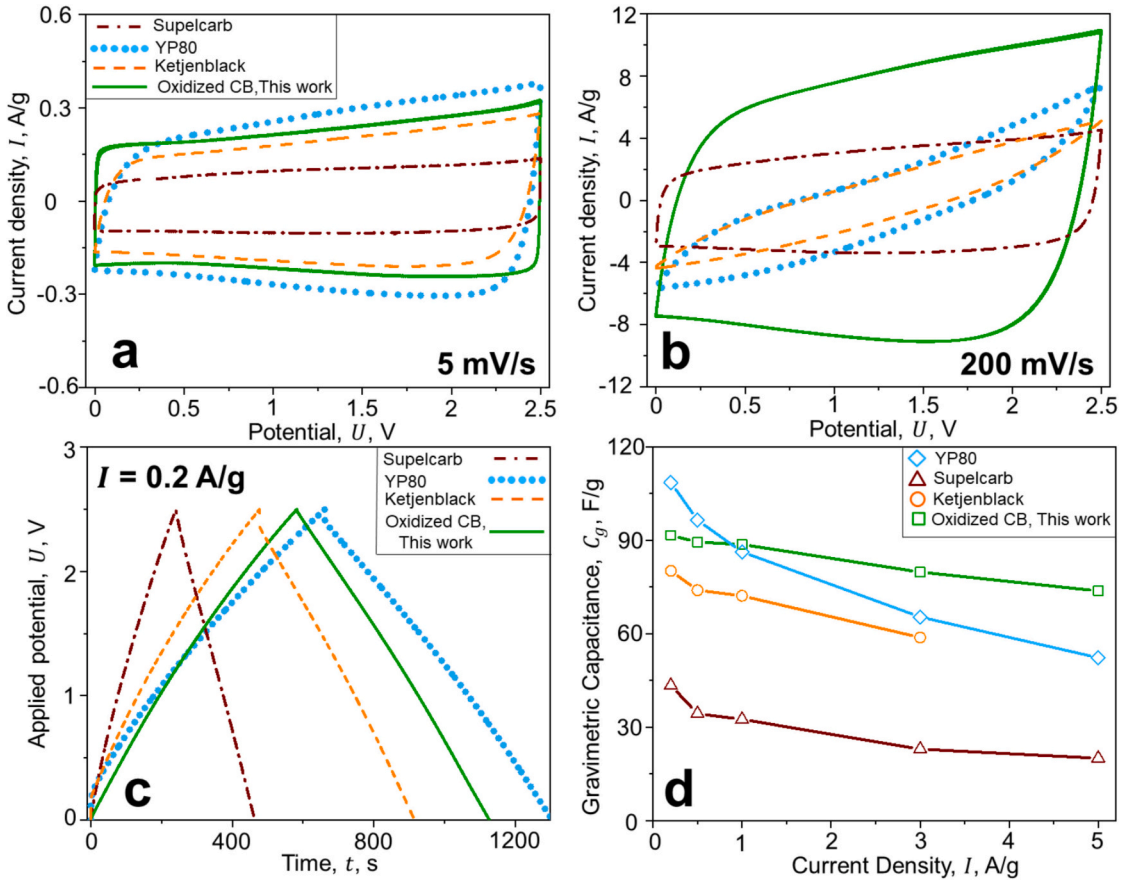

Fig. 4. Cyclic voltammograms with a scan rate of 5 (a) and 200 mV/s (b), galvanostatic charge-discharge curves at a current density, $I = 0.2$ A/g (c) and gravimetric capacitance, C_g, as a function of I (d) for CB (solid lines & squares, this work) oxidized at the conditions of Fig. 2 in comparison to those of Supelcarb (dot-broken lines & triangles), YP80 (dotted lines, diamonds) and Ketjenblack (broken lines & circles).

of microwave processing [58] and chemical activation of expensive graphite oxide (~200′000 $/kg) with liquid oxidizers [57], the ultra porous CB is produced here by oxidizing inexpensive commercial CB (few $/kg) in a 10 vol% O_2 atmosphere.

4. Conclusions

Here, ultra porous carbonaceous nanoparticles were prepared by judicious oxidation of commercial carbon black (CB) at 1200 °C in a 10 vol% O_2 in N_2 atmosphere. That way, it is shown that using high oxidation temperatures is essential for synthesis of ultra porous CBs that have superior EDLC performance than commercial ACs and CBs. Microscopy and X-Ray diffraction analysis revealed that CB nanoparticles become more disordered during oxidation at these conditions. The higher degree of disordering improves O_2 diffusion and enables the O_2 to react with the bulk CB, forming 2–8 nm pores. This increases the specific surface area, *SSA*, of CB by an order of magnitude, consistent with lattice Monte Carlo modelling of CB internal and external oxidation [31]. The resulting *SSA* of 2185 ± 199 m^2/g, obtained at 75 % conversion is twice to thrice larger than the *SSA* of CB oxidized at low temperatures [14,27]), 50–100 % larger than the *SSA* of most porous CB grades that are currently available in the market and on par with that of commercial activated carbons (ACs), e.g. YP80, commonly used in supercapacitors.

The electrochemical double layer capacitance of the oxidized CB is similar to the benchmark materials YP80 and Ketjenblack at lower rates ($I = 0.2$ A/g during GCPL and 5 mV/s during CV). However, at large scan rates and currents, the specific capacitance of the oxidized CB was 40 % larger than those of YP80 or Ketjenblack. This superior performance is attributed to the large concentration of pores with 2–8 nm radius formed by internal oxidation and lattice disordering of the present CB. Such pores cannot be produced at large concentrations by low temperature oxidation of CB [14,27] that is used widely to enhance the particle porosity. So, close control of the internal oxidation dynamics of CB is essential to design ultra porous carbonaceous nanomaterials and optimize their performance for electrochemical energy storage. In this regard, the data presented here can assist and facilitate the design and operation of large scale processes (i.e. ovens and flame reactors) for synthesis of ultra porous carbonaceous materials as it has been done even in our labs for nanomaterials from 0.01 kg/h [59] to over a kg/h [60].

Beyond, supercapacitors the ultra porous CB material might be useful as an effective lightweight conductive additive for Li-ion and post-Li-ion battery electrodes. For future battery technologies, such as conversion type metal-sulfur batteries, the high-surface area CB could also serve as an ideal conductive host with significant mesoporosity and optimized diffusion pathways for the sulfur/sulfide conversion reaction.

CRediT authorship contribution statement

Georgios A. Kelesidis: Writing – review & editing, Writing – original draft, Visualization, Validation, Supervision, Methodology, Investigation, Formal analysis, Conceptualization. **Nicola Rossi:** Validation, Investigation, Formal analysis. **Ayca Senol Gungor:** Writing – review & editing, Supervision, Methodology, Investigation, Formal analysis. **Christian Prehal:** Writing – review & editing, Supervision, Resources, Methodology. **Sotiris E. Pratsinis:** Writing – review & editing, Supervision, Resources, Project administration, Funding acquisition.

Declaration of competing interest

The authors declare that they have no known competing financial interests or personal relationships that could have appeared to influence the work reported in this paper.

Acknowledgements

This research was funded by the Particle Technology Laboratory, ETH Zurich and by the Swiss National Science Foundation (200020_182668, 250320_163243 and 206021_170729). We gratefully acknowledge the support of Dr. K. Rockstein (Orion Engineered Carbons) for providing the CB grades, Dr. F. Krumeich for microscopy imaging and Mr. A. Nagarkar for his support with TGA, N_2 adsoprtion and Raman spectroscopy measurements.

Appendix A. Supplementary data

Supplementary data to this article can be found online at https://doi.org/10.1016/j.powtec.2025.121557.

Data availability

Data will be made available on request.

References

[1] P. Roy, S.K. Srivastava, Nanostructured anode materials for lithium ion batteries, J Mater Chem A 3 (2015) 2454–2484, https://doi.org/10.1039/C4TA04980B.
[2] E. Frackowiak, F. Béguin, Carbon materials for the electrochemical storage of energy in capacitors, Carbon 39 (2001) 937–950, https://doi.org/10.1016/S0008-6223(00)00183-4.
[3] P. Simon, Y. Gogotsi, Perspectives for electrochemical capacitors and related devices, Nat. Mater. 19 (2020) 1151–1163, https://doi.org/10.1038/s41563-020-0747-z.
[4] Z. Lin, E. Goikolea, A. Balducci, K. Naoi, P.L. Taberna, M. Salanne, G. Yushin, P. Simon, Materials for supercapacitors: when Li-ion battery power is not enough, Mater. Today 21 (2018) 419–436, https://doi.org/10.1016/j.mattod.2018.01.035.
[5] P. Simon, Y. Gogotsi, Materials for electrochemical capacitors, Nat. Mater. 7 (2008) 845–854, https://doi.org/10.1038/nmat2297.
[6] S. Modi, O. Okonkwo, S. Saha, M.B. Foston, P. Biswas, Reuse of lignin to synthesize high surface area carbon nanoparticles for supercapacitors using a continuous and single-step aerosol method, ACS Nano 17 (2023) 17048–17057, https://doi.org/10.1021/acsnano.3c04443.
[7] F. Caturla, M. Molinasabio, F. Rodriguezreinoso, Preparation of activated carbon by chemical activation with $ZnCl_2$, Carbon 29 (1991) 999–1007, https://doi.org/10.1016/0008-6223(91)90179-M.
[8] P. Ehrburger, A. Addoun, F. Addoun, J.B. Donnet, Carbonization of coals in the presence of alkaline hydroxides and carbonates - formation of activated carbons, Fuel 65 (1986) 1447–1449, https://doi.org/10.1016/0016-2361(86)90121-3.
[9] J.A. Maciá-Agulló, B.C. Moore, D. Cazorla-Amorós, A. Linares-Solano, Activation of coal tar pitch carbon fibres: physical activation vs. chemical activation, Carbon 42 (2004) 1367–1370, https://doi.org/10.1016/j.carbon.2004.01.013.
[10] J. Laine, A. Calafat, M. Labady, Preparation and characterization of activated carbons from coconut shell impregnated with phosphoric-acid, Carbon 27 (1989) 191–195, https://doi.org/10.1016/0008-6223(89)90123-1.
[11] Z.H. Hu, E.F. Vansant, Synthesis and characterization of a controlled micropore-size carbonaceous adsorbent produced from walnut shell, Microporous Mater. 3 (1995) 603–612, https://doi.org/10.1016/0927-6513(94)00067-6.
[12] J. Rodriguez-Mirasol, T. Cordero, J.J. Rodriguez, Preparation and characterization of activated carbons from Eucalyptus Kraft lignin, Carbon 31 (1993) 87–95, https://doi.org/10.1016/0008-6223(93)90160-C.
[13] N. Kostoglou, C. Koczwara, C. Prehal, V. Terziyska, B. Babic, B. Matovic, G. Constantinides, C. Tampaxis, G. Charalambopoulou, T. Steriotis, S. Hinder, M. Baker, K. Polychronopoulou, C. Doumanidis, O. Paris, C. Mitterer, C. Rebholz, Nanoporous activated carbon cloth as a versatile material for hydrogen adsorption, selective gas separation and electrochemical energy storage, Nano Energy 40 (2017) 49–64, https://doi.org/10.1016/j.nanoen.2017.07.056.
[14] C.W. Fan, Y. Dong, Y.F. Liu, L.H. Zhang, D.K. Wang, X.J. Lin, Y. Lv, S. Zhang, H. H. Song, D.Z. Jia, Mesopore-dominated hollow carbon nanoparticles prepared by simple air oxidation of carbon black for high mass loading supercapacitors, Carbon 160 (2020) 328–334, https://doi.org/10.1016/j.carbon.2020.01.034.
[15] C. Prehal, C. Koczwara, N. Jäckel, A. Schreiber, M. Burian, H. Amenitsch, M. A. Hartmann, V. Presser, O. Paris, Quantification of ion confinement and desolvation in nanoporous carbon supercapacitors with modelling and X-ray scattering, Nat. Energy 2 (2017) 16215, https://doi.org/10.1038/nenergy.2016.215.
[16] P. Li, H. Li, D.L. Han, T.X. Shang, Y.Q. Deng, Y. Tao, W. Lv, Q.H. Yang, Packing activated carbons into dense graphene network by capillarity for high volumetric performance supercapacitors, Adv. Sci. 6 (2019) 1802355, https://doi.org/10.1002/advs.201802355.
[17] G. Wang, Z.L. Lu, Y. Li, L.H. Li, H.F. Ji, A. Feteira, D. Zhou, D.W. Wang, S.J. Zhang, I.M. Reaney, Electroceramics for high-energy density capacitors: current status and future perspectives, Chem. Rev. 121 (2021) 6124–6172, https://doi.org/10.1021/acs.chemrev.0c01264.

[18] A.B. Fuertes, F. Pico, J.M. Rojo, Influence of pore structure on electric double-layer capacitance of template mesoporous carbons, J. Power Sources 133 (2004) 329–336, https://doi.org/10.1016/j.jpowsour.2004.02.013.
[19] O. Waser, R. Büchel, A. Hintennach, P. Novák, S.E. Pratsinis, Continuous flame aerosol synthesis of carbon-coated nano-$LiFePO_4$ for Li-ion batteries, J. Aerosol Sci. 42 (2011) 657–667, https://doi.org/10.1016/j.jaerosci.2011.06.003.
[20] www.chemanalyst.com/industry-report/carbon-black-market-440.
[21] G.A. Kelesidis, S. Benz, S.E. Pratsinis, Process design for carbon black size and morphology, Carbon 213 (2023) 118255, https://doi.org/10.1016/j.carbon.2023.118255.
[22] A. Krause, P. Kossyrev, M. Oljaca, S. Passerini, M. Winter, A. Balducci, Electrochemical double layer capacitor and lithium-ion capacitor based on carbon black, J. Power Sources 196 (2011) 8836–8842, https://doi.org/10.1016/j.jpowsour.2011.06. 019.
[23] S. Khodabakhshi, P.F. Fulvio, E. Andreoli, Carbon black reborn: structure and chemistry for renewable energy harnessing, Carbon 162 (2020) 604–649, https://doi.org/10.1016/j.carbon.2020.02.058.
[24] F. Beck, M. Dolata, E. Grivei, N. Probst, Electrochemical supercapacitors based on industrial carbon blacks in aqueous H_2SO_4, J. Appl. Electrochem. 31 (2001) 845–853, https://doi.org/10.1023/A:1017529920916.
[25] D. Pech, M. Brunet, H. Durou, P.H. Huang, V. Mochalin, Y. Gogotsi, P.L. Taberna, P. Simon, Ultrahigh-power micrometre-sized supercapacitors based on onion-like carbon, Nat. Nanotechnol. 5 (2010) 651–654, https://doi.org/10.1038/nnano.2010.162.
[26] G.S. Jiang, J. Guo, Y.Z. Sun, X.G. Liu, J.Q. Pan, Pyrolytic carbon black-derived porous carbon with spherical skeleton as recovered and enduring electrode material for supercapacitor, J Energy Storage 44 (2021) 103372, https://doi.org/10.1016/j.est.2021.103372.
[27] G.A. Kelesidis, N. Rossi, S.E. Pratsinis, Porosity and crystallinity dynamics of carbon black during internal and surface oxidation, Carbon 197 (2022) 334–340, https://doi.org/10.1016/j.carbon.2022.06.020.
[28] D. Tashima, H. Yoshitama, M. Otsubo, S. Maeno, Y. Nagasawa, Evaluation of electric double layer capacitor using Ketjenblack as conductive nanofiller, Electrochim. Acta 56 (2011) 8941–8946, https://doi.org/10.1016/j.electacta.2011.07.124.
[29] N. Chanut, D. Stefaniuk, J.C. Weaver, Y. Zhu, Y. Shao-Horn, A. Masic, F.J. Ulm, Carbon-cement supercapacitors as a scalable bulk energy storage solution, PNAS 120 (2023) e2304318120, https://doi.org/10.1073/pnas.2304318120.
[30] G.A. Kelesidis, S.E. Pratsinis, Estimating the internal and surface oxidation of soot agglomerates, Combust. Flame 209 (2019) 493–499, https://doi.org/10.1016/j.combustflame. 2019.08.001.
[31] G.A. Kelesidis, P. Crepaldi, M.S.E. Pratsinis, Oxidation dynamics of soot or carbon black accounting for its core-shell structure and pore network, Carbon 219 (2024) 118264, https://doi.org/10.1016/j.carbon.2023.118764.
[32] P. Gilot, F. Bonnefoy, F. Marcuccilli, G. Prado, Determination of kinetic data for soot oxidation - modeling of competition between oxygen diffusion and reaction during thermogravimetric analysis, Combust. Flame 95 (1993) 87–100, https://doi.org/10.1016/0010-2180(93)90054-7.
[33] G. Kühner, M. Voll, Manufacture of carbon black, in: J.-B. Donnet, R.C. Bansal, M. J. Wang (Eds.), Carbon Black-Science and Technology, 2nd edition, Marcel Dekker, New York, NY, 1993.
[34] S. Brunauer, P.H. Emmett, E. Teller, Adsorption of gases in multimolecular layers, J. Am. Chem. Soc. 60 (1938) 309–319, https://doi.org/10.1021/ja01269a023.
[35] E.P. Barrett, L.G. Joyner, P.P. Halenda, The determination of pore volume and area distributions in porous substances. 1. Computations from nitrogen isotherms, J. Am. Chem. Soc. 73 (1951) 373–380, https://doi.org/10.1021/ja01145a126.
[36] J. Jagiello, J. Kenvin, J.P. Olivier, A.R. Lupini, C.I. Contescu, Using a new finite slit pore model for NLDFT analysis of carbon pore structure, Adsorpt. Sci. Technol. 29 (2011) 769–780, https://doi.org/10.1260/0263-6174.29.8.769.
[37] N. Iwashita, C.R. Park, H. Fujimoto, M. Shiraishi, M. Inagaki, Specification for a standard procedure of X-ray diffraction measurements on carbon materials, Carbon 42 (2004) 701–714, https://doi.org/10.1016/j.carbon.2004.02.008.
[38] M. Lapuerta, F. Oliva, J.R. Agudelo, A.L. Boehman, Effect of fuel on the soot nanostructure and consequences on loading and regeneration of diesel particulate filters, Combust. Flame 159 (2012) 844–853, https://doi.org/10.1016/j.combustflame.2011.09. 003.
[39] A. Sadezky, H. Muckenhuber, H. Grothe, R. Niessner, U. Pöschl, Raman micro spectroscopy of soot and related carbonaceous materials: spectral analysis and structural information, Carbon 43 (2005) 1731–1742, https://doi.org/10.1016/j.carbon.2005.02.018.
[40] A. Baldelli, S.N. Rogak, Morphology and Raman spectra of aerodynamically classified soot samples, Atmos. Meas. Tech. 12 (2019) 4339–4346, https://doi.org/10.5194/amt-12-4339-2019.
[41] M.D. Stoller, R.S. Ruoff, Best practice methods for determining an electrode material's performance for ultracapacitors, Energ, Environ. Sci. 3 (2010) 1294–1301, https://doi.org/10.1039/C0EE00074D.
[42] M.L. Botero, Y. Sheng, J. Akroyd, J. Martin, J.A.H. Dreyer, W.M. Yang, M. Kraft, Internal structure of soot particles in a diffusion flame, Carbon 141 (2019) 635–642, https://doi.org/10.1016/j.carbon.2018.09.063.
[43] Q.H. Chang, R. Gao, M. Gao, G.S. Yu, F.C. Wang, The structural evolution and fragmentation of coal-derived soot and carbon black during high-temperature air oxidation, Combust. Flame 216 (2020) 111–125, https://doi.org/10.1016/j.combustflame. 2019.11.045.
[44] A. Antidormi, S. Roche, L. Colombo, Impact of oxidation morphology on reduced graphene oxides upon thermal annealing, J. Phys. Mater. 3 (2020) 015011, https://doi.org/10.1088/2515-7639/ab5ef2.
[45] G.A. Kelesidis, A. Nagarkar, P.G. Rivano, Solar steam generation enabled by carbon black: the impact of particle size and nanostructure, AICHE J. 70 (2024) e18619, https://doi.org/10.1002/aic.18619.
[46] www.nouryon.com/product/ketjenblack-ec-600jd-electroconductive-carbon-black-cas-1333-86-4.
[47] D.P. Singh, D. Chandra, V. Vishal, B. Hazra, P. Sarkar, Impact of degassing time and temperature on the estimation of pore attributes in shale, Energy Fuel 35 (2021) 15628–15641, https://doi.org/10.1016/S0008-6223(99)00143-8.
[48] M. Seredych, J. Jagiello, T.J. Bandosz, Complexity of CO_2 adsorption on nanoporous sulfur-doped carbons - is surface chemistry an important factor? Carbon 74 (2014) 207–217, https://doi.org/10.1016/j.carbon.2014.03.024.
[49] J.L. Zhao, H. Xu, D.Z. Tang, J.P. Mathews, S. Li, S. Tao, A comparative evaluation of coal specific surface area by CO_2 and N_2 adsorption and its influence on CH_4 adsorption capacity at different pore sizes, Fuel 183 (2016) 420–431, https://doi.org/10.1016/j.fuel.2016.06.076.
[50] J. van den Broek, I.C. Weber, A.T. Güntner, S.E. Pratsinis, Highly selective gas sensing enabled by filters, Mater. Horiz. 8 (2021) 661–684, https://doi.org/10.1039/D0MH01453B.
[51] J.E. Shields, S. Lowell, A method for the estimation of micropore volume and micropore surface-area, Powder Technol. 36 (1983) 1–4, https://doi.org/10.1016/0032-5910(83)80001-1.
[52] L. Mädler, A.A. Lall, S.K. Friedlander, One-step aerosol synthesis of nanoparticle agglomerate films: simulation of film porosity and thickness, Nanotechnology 17 (2006) 4783–4795, https://doi.org/10.1088/0957-4484/17/19/001.
[53] R. Neffati, J.M.C. Brokken-Zijp, Structure and porosity of conductive carbon blacks, Mater. Chem. Phys. 260 (2021) 124177, https://doi.org/10.1016/j.matchemphys.2020.124177.
[54] D. Boonpakdee, C.F.G. Yévenes, W. Surareungchai, C. La-o-vorakiat, Exploring non-linearities of carbon-based microsupercapacitors from an equivalent circuit perspective, J Mater Chem A 6 (2018) 7162–7167, https://doi.org/10.1039/C8TA01995A.
[55] M. Seredych, D. Hulicova-Jurcakova, G.Q. Lu, T.J. Bandosz, Surface functional groups of carbons and the effects of their chemical character, density and accessibility to ions on electrochemical performance, Carbon 46 (2008) 1475–1488, https://doi.org/10.1016/j.carbon.2008.06.027.
[56] G.P. Wang, L. Zhang, J.J. Zhang, A review of electrode materials for electrochemical supercapacitors, Chem. Soc. Rev. 41 (2012) 797–828, https://doi.org/10.1039/C1CS15060J.
[57] Y.W. Zhu, S. Murali, M.D. Stoller, K.J. Ganesh, W.W. Cai, P.J. Ferreira, A. Pirkle, R. M. Wallace, K.A. Cychosz, M. Thommes, D. Su, E.A. Stach, R.S. Ruoff, Carbon-based supercapacitors produced by activation of graphene, Science 332 (2011) 1537–1541, https://doi.org/10.1126/science.1200770.
[58] Y.W. Zhu, S. Murali, M.D. Stoller, A. Velamakanni, R.D. Piner, R.S. Ruoff, Microwave assisted exfoliation and reduction of graphite oxide for ultracapacitors, Carbon 48 (2010) 2118–2122, https://doi.org/10.1016/j.carbon.2010.02.001.
[59] L. Mädler, H.K. Kammler, R. Mueller, S.E. Pratsinis, Controlled synthesis of nanostructured particles by flame spray pyrolysis, J. Aerosol Sci. 33 (2002) 369–389, https://doi.org/10.1016/S0021-8502(01)00159-8.
[60] R. Mueller, L. Mädler, S.E. Pratsinis, Nanoparticle synthesis at high production rates by flame spray pyrolysis, Chem. Eng. Sci. 58 (2003) 1969–1976, https://doi.org/10.1016/S0009-2509(03)00022-8.